

# X-ray Microscopy and Talbot Imaging with the Matter in Extreme Conditions X-ray Imager at LCLS

Eric Galtier<sup>1</sup>, Hae Ja Lee<sup>1</sup>, Dimitri Khaghani<sup>1</sup>, Nina Boiadjieva<sup>1</sup>, Peregrine McGehee<sup>1</sup>, Ariel Arnott<sup>1</sup>, Brice Arnold<sup>1</sup>, Meriame Berboucha<sup>1,2</sup>, Eric Cunningham<sup>1</sup>, Nick Czapla<sup>1</sup>, Gilliss Dyer<sup>1</sup>, Bob Ettlbrick<sup>1</sup>, Philip Hart<sup>1</sup>, Phil Heimann<sup>1</sup>, Marc Welch<sup>1</sup>, Mikako Makita<sup>3</sup>, Arianna E. Gleason<sup>1</sup>, Silvia Pandolfi<sup>1,4</sup>, Anne Sakdinawat<sup>1</sup>, Yanwei Liu<sup>1</sup>, Michael J. Wojcik<sup>6</sup>, Daniel Hodge<sup>6</sup>, Richard Sandberg<sup>6</sup>, Frank Seiboth<sup>7</sup>, Bob Nagler<sup>1</sup>

1. SLAC National Accelerator Laboratory,  
2575 Sand Hill Rd., Menlo Park, CA 94025, USA.

2. Imperial College London, Plasma Physics,  
London, SW7 2AZ, United Kingdom

3. European XFEL, Holzkoppel 4, 22869 Schenefeld, Germany

4. Sorbonne University, Paris, France

5. Argonne National Laboratory,  
9700 S. Cass Avenue Lemont, IL 60439

6. Brigham Young University,  
Department of Physics and Astronomy, Provo, UT, 84602, USA

7. Center for X-ray and Nano Science,  
Deutsches Elektronen-Synchrotron DESY,  
Notkestraße 85, DE-22607 Hamburg, Germany

(Dated: November 19, 2024)

The last decade has shown the great potential that X-ray Free Electron Lasers (FEL) have to study High Energy Density (HED) matter. Experiments at FELs have made significant breakthroughs in Shock Physics and Dynamic Diffraction, Dense Plasma Physics and Warm Dense Matter Science, using techniques such as isochoric heating, inelastic scattering, small angle scattering and x-ray diffraction. In addition, and complementary to these techniques, the coherent properties of the FEL beam can be used to image HED samples with high fidelity. We present new imaging diagnostics and techniques developed at the Matter in Extreme Conditions (MEC) instrument at Linac Coherent Light Source (LCLS) over the last few years. We show results in Phase Contrast Imaging geometry, where the X-ray beam propagates from the target to a camera revealing its phase, as well as in Direct Imaging geometry, where a real image of the sample plane is produced in the camera with a spatial resolution down to 200 nm. Last, we show an implementation of the Talbot Imaging method allowing both x-ray phase and intensity measurements change introduced by a target with sub-micron resolution.

## I. INTRODUCTION

High Energy Density (HED) science has traditionally made ample use of X-ray radiography and imaging to investigate a variety of phenomena, such as the implosions of inertial confinement fusion (ICF) capsules [1–6], X-pinch plasmas [7] and the general hydrodynamics of evolution of HED targets. [8, 9]. Since the dynamics of these phenomena evolve on very fast time scales (from femtoseconds to nanoseconds), ultrashort X-ray pulses are needed to obtain quantitative data. Historically, X-ray sources generated by the interaction of high power laser with backlighter targets have been employed, with typical spatial and temporal resolution on the order of tens of micrometers and hundreds of picoseconds or more [8, 10] Phase Contrast Imaging techniques with back-lighters have also been developed [11–14], albeit with limited resolutions compared to synchrotrons, where sub-micron resolutions are standard [15, 16].

The start of operation of LCLS [17] in 2009 opened new possibilities for X-ray imaging in HED science. The coherent properties of the beam allow for imaging with sub-micron spatial resolution, while the short, bright pulses allow temporal resolution of tens of femtoseconds. These combined properties allow for single-shot X-ray imaging techniques to emerge as a leading technique to further our understanding of

complex HED phenomena. At LCLS, the Matter in Extreme Conditions end-station [18] is specifically tailored to field experiments in HED science. To foster this field of research, the different imaging techniques and instruments have been developed, and are available to its user community.

In this paper, we describe the use and performances of the MEC Xray Imager (MXI) and the different diagnostic imaging techniques that make use of it, and present preliminary proof of principle experiments to showcase its potential for HED science.

## II. INSTRUMENT OVERVIEW

The MXI instrument has two main components: an in-vacuum X-ray lens stack holder and an in-air optical microscope, as detailed in Figure 1.

The in-vacuum component is designed for use in the MEC target chamber (technical details on the endstation can be found in [18]). It uses compound refractive Beryllium lenses (Be CRL) to focus the X-ray beam to sub-micron spot sizes. The capabilities of such lens stacks have been described extensively in the literature [19–22], and have been used for this purpose at MEC [23–25]. A stack of lenses is placed on alignment stages that positions the lenses in the beam. Up to three

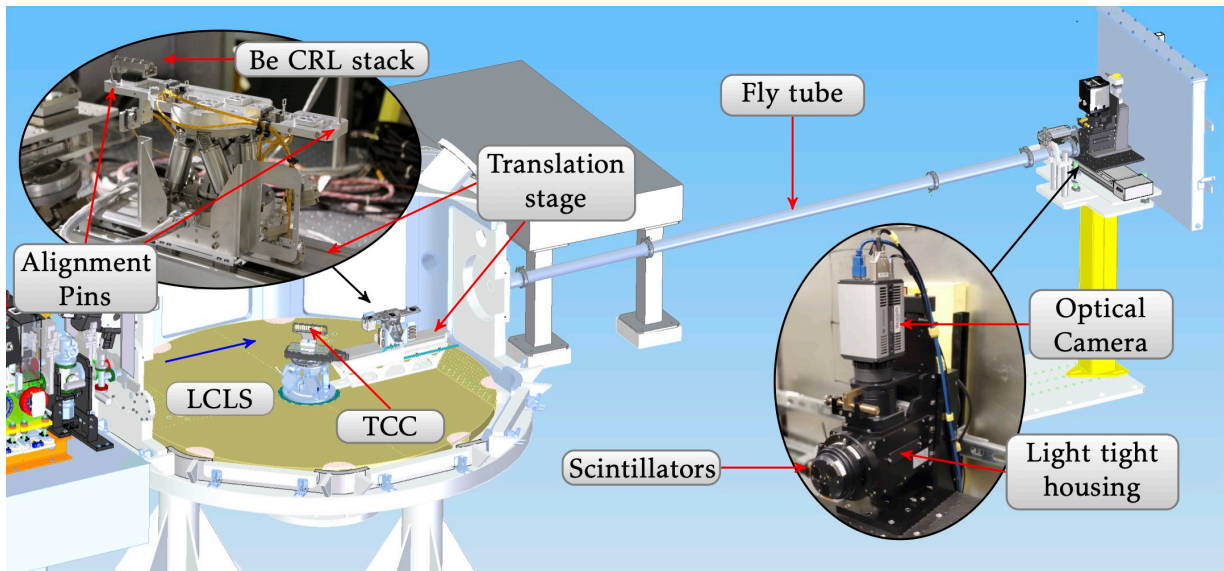


FIG. 1. Overview of the MXI system at MEC in Direct Imaging geometry with the indirect X-ray detector placed about 4 m from TCC behind a fly tube. TCC is Target Chamber Center, the interaction point between the LCLS and the optical lasers.

stacks of lenses can be placed on the instrument simultaneously, to allow usage of different photon energies and/or focal lengths during an experiment without venting the MEC vacuum chamber. The front stack can accommodate up to 100 lenses, necessary for the higher photon energies. The lens stacks are mounted on a hexapod, allowing for precise alignment with six degrees of freedom: the translations are aligned with the LCLS orthogonal coordinate system and rotation around each of these axis. The hexapod is attached to a linear translation stage with 500 mm travel range to change the distance between the lens stack and the object plane along the LCLS X-ray beam.

Two thin pins are precisely located with respect to the Be CRL stacks on the lens platform and are far from each other along the FEL direction to maximize alignment accuracy. They are initially used for the pre-alignment in air with the reference optical laser collinear with the FEL, and later, in vacuum conditions using the FEL itself via their shadowgraphy on the detector. These pins are critical to allow for a fast while precise alignment, typically achieved in less than thirty minutes.

Since stacks of Be lenses are known to have aberrations, which can limit their use in imaging and phase contrast application, a phase plate that corrects these aberrations [25] can be placed 10 mm in front of the lens set. The phase plate is aligned in the horizontal and vertical direction with two small linear stages, which can also completely retract the corrector. The MXI lens sets can be placed either upstream of the sample (see Sec.III) for phase contrast imaging or downstream (see Sec.IV) for direct imaging of a sample.

In typical HED experiments, samples are driven by the MEC short or long pulse laser orthogonally to the imaging direction (e.g., a shock is imaged traveling through a sample). To this end a sample holder allowing such geometry is available (see Fig. 2).

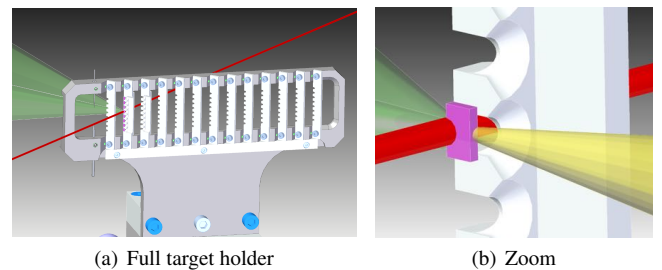


FIG. 2. (a) 3D model of the target holder with an orthogonal configuration between the long pulse drive laser (in green) and the X-rays (in red). (b) zoom in of a single target on a pillar suitable for use with the MEC VISAR diagnostic [18] (VISAR beam in yellow).

The samples are aligned to TCC with better than  $20 \mu\text{m}$  accuracy using two long-distance telescopes (see [18] for details), which view the sample at orthogonal directions. The MXI can be used to further improve the alignment accuracy down to better than  $1 \mu\text{m}$  in the plan perpendicular to the FEL. The samples are mounted on a pillar that is screwed to the sample holder. The pillars are designed to accommodate for line of sight of additional scientific diagnostics (e.g. for use in shock experiment to allow for VISAR [26] measurements on thin samples).

The image is recorded on the in-air component of the MXI, an X-ray camera that is placed behind the MEC chamber. The camera can be placed between 1.3 m to 4.3 m behind the sample plane. For the large propagation distance, a fly tube is inserted and terminated by a  $125 \mu\text{m}$  thick kapton window to maintain low scattering and absorption transport conditions for the X-ray beam. In general, the farthest distance is preferred to have the largest magnification, although some ap-

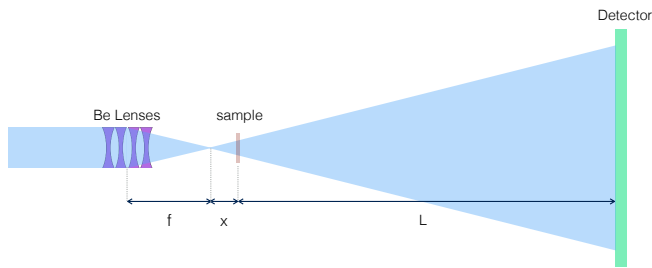


FIG. 3. Sketch of the MXI setup in phase contrast imaging (PCI) geometry.

plication may benefit from the shorter distance (i.e., ptychography [27]). For most experiments, we have used an indirect X-ray imaging Optique Peter microscope [28], consisting of three options of Ce:GAG scintillators and three options of high-numerical aperture infinity-corrected optical microscope objectives ( $\times 2$ ,  $\times 4$  and  $\times 10$  magnification) to further chose between high-magnification or large field-of-view. This assembly is coupled to an Andor Zyla 5.5 sCMOS optical camera, which has a pixel size of  $6.5 \mu\text{m}$ . Direct imaging cameras (e.g., ePix or Jungfrau) can be used instead, however the resolution is limited by the pixel size ( $100 \mu\text{m}$  for ePix10k,  $50 \mu\text{m}$  for ePix100 and  $75 \mu\text{m}$  for Jungfrau). In addition, multiframe X-ray cameras developed by hCMOS [29] with pixel size of  $25 \mu\text{m}$ , [30–32] and capable of capturing multiple image frames spaced as little as 2 ns apart, can also be used, in conjunction with the LCLS multi-bunch operation mode [33, 34]. An advantage of direct detection compared to scintillator based detection is that these cameras are orders of magnitude more sensitive, and therefore can be used with thicker, higher Z, more absorbent samples.

### III. PHASE CONTRAST IMAGING GEOMETRY

The imaging geometry first deployed at MEC [35] used a diverging beam at target and optic-free propagation from target to detector plane. A schematic of the setup can be seen in Fig.3.

The MXI, with a lens set of focal length  $f$ , is placed in the MEC vacuum chamber and focuses the LCLS beam to approximately 100 nm. A certain distance,  $x$ , behind the focus, a sample is placed in the divergent beam. The X-ray beam propagates to a detector at a distance  $L$  behind the sample, leading to a geometric magnification of the sample of  $\frac{L}{x}$ . Due to the long propagation distance of the X-ray, phase difference induced by the sample can readily be seen in the image (e.g., clear fringes appear at sharp phase boundaries). Iterative algorithms can be used to retrieve the phase, and if this is successful, the full complex transmission function (i.e., absorption and phase shift) can be calculated. Experiment in this geometries have been fielded at MEC, yielding scientific results on shockwave propagation in diamond [35] and the kinetics of phase transformations in silicon [36]. The setup can be easily combined with X-ray diffraction. Moving the lenses of the

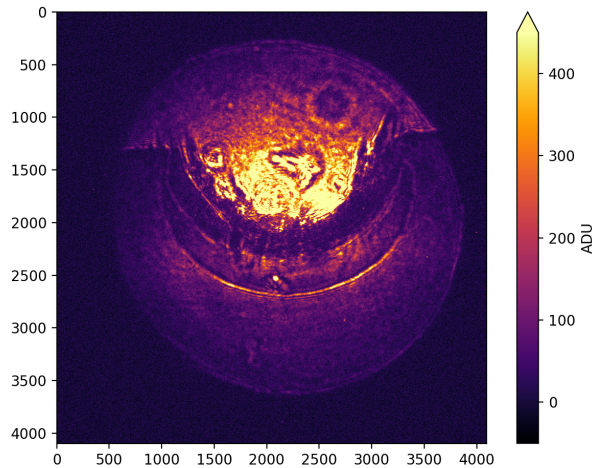


FIG. 4. The MEC long pulse laser impinges on a plastic ablator coated on a Si target. An elastic shock front, followed by a plastic deformation front indicative of material compression travels from top to bottom. Ablator ejecta coming out of the vacuum-ablator interface are also observed.

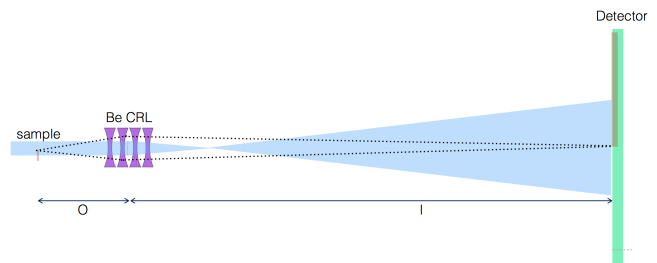


FIG. 5. MXI in direct imaging geometry.

MXI closer to the target reduced the field of view of the image, and therefore the area where X-rays hit the target. In this way, diffraction from an area of only a few microns in size can be obtained, and different crystallographic phases in the sample can be identified [36]. A typical image of a laser-generated shock wave traveling through a sample can be seen in Fig. 4 and more examples have been published in e.g., [18, 23, 35]

### IV. DIRECT IMAGING GEOMETRY

While the PCI geometry described above has great potential when a full phase retrieval can be performed, it proves to be challenging for HED samples. Without such a phase retrieval, the resolution can be severely limited, and an alternative setup that directly images a sample on the detector has been developed and used at MEC. A sketch of the setup is shown in Figure 5.

In this geometry the Be lenses are placed behind the sample such that the distance to the sample,  $O$ , and the distance to the camera,  $I$ , matches the well known thin lens formula  $\frac{1}{O} + \frac{1}{I} = \frac{1}{f}$ , with  $f$  the focal length of the Be lenses. Such a setup allows

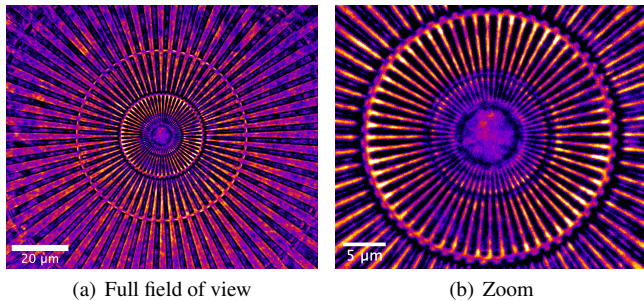


FIG. 6. Image of a Siemens star resolution target at 9.5 keV in a false color scale. (a) Full field of view of  $110 \mu\text{m} \times 93 \mu\text{m}$ . (b) zoom of the center. The smallest features near the center of the picture have a spacing of 200 nm, resulting in an effective pixel size of about 0.045 nm/px.

for imaging intensity contrast of the sample with sub-micron resolution, even when phase reconstruction is not possible.

The MXI instrument was tested in the direct imaging geometry at 8.2 keV, 9.5 keV and 18 keV photon energy. For 8.2 keV and 9.5 keV, a set of 25 Beryllium lenses with a curvature of  $50 \mu\text{m}$  were used. At 8.2 keV (9.5 keV), the set has a focal length of 204 mm (264 mm) and was placed 214 mm (281 mm) downstream of the target, leading to an image at the detector, placed 4.3 m behind the lenses, with a magnification of approximately  $\times 20$  ( $\times 15$ ). The position of the lenses was tuned to get the best imaging resolution, using resolution targets. Images of the resolution target are shown in Fig.6. Line widths as small as 200 nm can be clearly resolved.

At photon energies as high as 18 keV, the setup and alignment is more sensitive since many more Be lenses are needed. In addition, the shortest focal length that can be used is generally larger, leading to a smaller magnification. Nevertheless, the higher photon energy allows using either thicker targets, or targets containing higher Z-elements, while maintaining enough transmission to collect high-quality images. We demonstrated its use with a lens stack of 98 lenses of  $50 \mu\text{m}$  radius of curvature at their apex, leading to a focal length of 266 mm and a magnification of  $\times 15$ . Measurement on resolution targets showed a resolution similar to 8.2 keV and 9.5 keV.

Examples of the use of the MXI in direct imaging geometry are detailed below. In Figure 7 a shockwave in a silicon sample, driven by the MEC short pulse laser is depicted.

This geometry is compatible with both the long pulse and the short pulse laser systems available at MEC, as well as a suite of X-ray and optical diagnostics (e.g. X-ray Diffraction, VISAR, X-ray spectroscopy, optical polarimetry) making it an ideal technique to obtain a complete picture of the dynamics happening in HED samples.

The imaging setup can also be used to measure the spot size of the standard beryllium focusing lenses that are in the MEC beamline. These lenses sit approximately 4.2 m upstream of the center of the MEC target chamber (see [18] for details), and therefore a stack with focal length between 3.9 m and

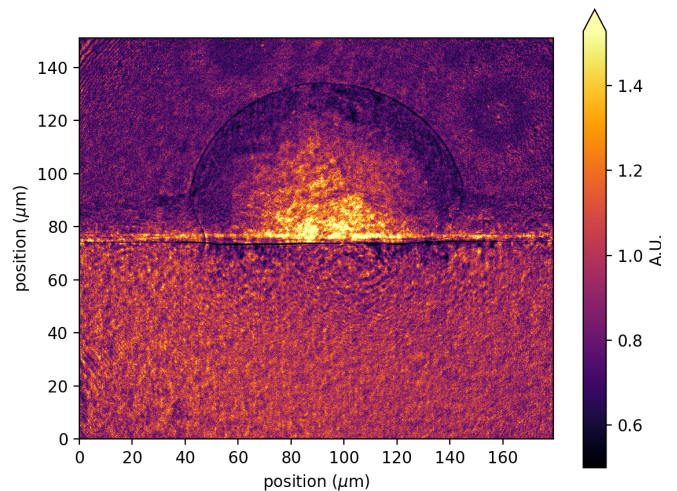


FIG. 7. White-Field corrected image of a shock wave propagating through a silicon sample. The MEC short pulse laser, with pulse length of 45 fs and energy of 1 J was focused down to a spot of  $7 \mu\text{m}$  diameter on the edge of a Si wafer,  $100 \mu\text{m}$  thick in the X-ray direction. The image is taken 2 ns after the laser strikes the target. We can clearly observe the propagation of the near-spherical expanding shock wave originating from the laser/surface interaction, as well as compressed (darker) material just behind the shock front. The target is set between about 70 and  $150 \mu\text{m}$  on the vertical axis, while the rest is vacuum.

4.4 m is generally used for standard MEC experiment, with a best focus around  $1.2 \mu\text{m}$ . Wavefront measurement have in the past been performed of such lens stack, showing significant spherical aberrations, generating ring-patterns around the focus [37]. The MXI direct imaging geometry can be used to image the intensity profile of the X-ray beam on the sample. In Figure 8, we show the intensity profile around the focus of our beamline lenses as imaged by the MXI instrument.

The airy-like ring pattern can be clearly seen. This type of measurement is of importance for all optical pump – X-ray probe experiments where X-rays are usually being used out of focus in the hope of illuminating a more uniform area. Our high-resolution imager shows, through the measurement of the X-ray caustic profile, that it might not be the case.

Table I summarizes the working envelop of the MXI and its expected performances in direct imaging mode. The device can provide high resolution X-ray imaging over the full X-ray energy range available at MEC, albeit at varying resolution and magnification which are a function of the incoming photon energy. The total magnification is a combination of the X-ray magnification provided by the Be CRL in vacuum (this mainly constraints the diffraction limited performances), and the optical magnification provided by the objective used in the Optique Peter assembly (this allow for oversampling of the X-ray images).

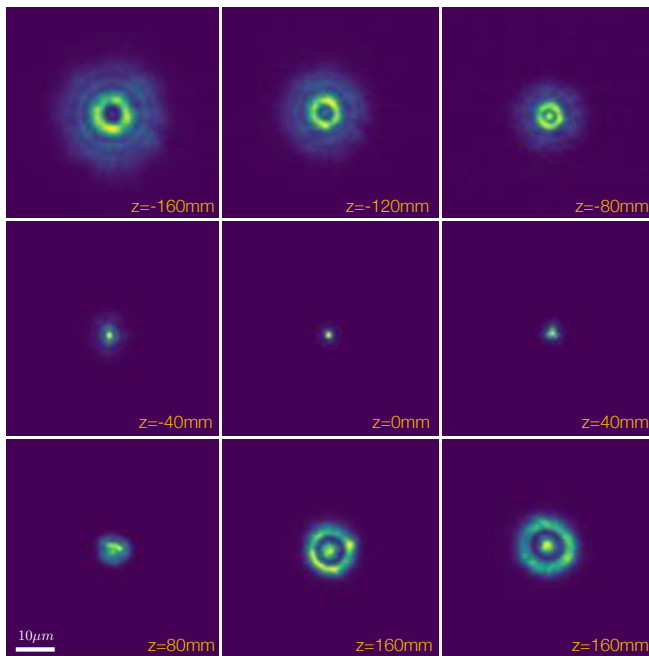


FIG. 8. Intensity profile of the focus of the MEC beamline lenses in steps of 40 mm. A set of 7 Be lenses with curvature of  $300\ \mu\text{m}$  at their apex, leading to a focal length of 4.22 m was chosen.  $800\ \mu\text{m}$  pinhole were placed in before and after the lens set to restrict the X-ray to the useful aperture of the lenses.

TABLE I. Summary of the specifications of the MXI.

Parameter	Value	Unit
Photon Energy	5 – 24	keV
Repetition Rate	On demand – 120 <sup>a</sup>	Hz
Pulse Duration	< 20 – 50	fs
X-ray magnification	$\times 5 - \times 40$	-
Total magnification <sup>b</sup>	$\times 7 - \times 400$	-
Field of View	50 – 300	$\mu\text{m}$
Beam mode	SASE, seeded <sup>c</sup> , multipulse <sup>d</sup>	-

<sup>a</sup> 120 Hz is compatible with X-ray cameras only. It is typically used at 30 Hz maximum for alignment. Otherwise, it matches the optical laser repetition rate.

<sup>b</sup> Combination of X-ray and Optical magnification.

<sup>c</sup> Reduces chromatic aberrations but lower the input X-ray pulse energy.

<sup>d</sup> With use of the hCMOS detector.

## V. TALBOT IMAGING

A special capability of using the MXI in direct imaging mode is his compatibility with Talbot interferometry. In this configuration, the phase accumulated by the X-ray pulse when transporting through the sample can be measured. When coupled to a phase retrieval method, this configuration has the advantage to help the removal of artifacts introduced by the use of the Be CRL. These artifacts are introduced by the density inhomogeneities of each transmissive Be lens from the stack. Some of these structures can be treated by a simple

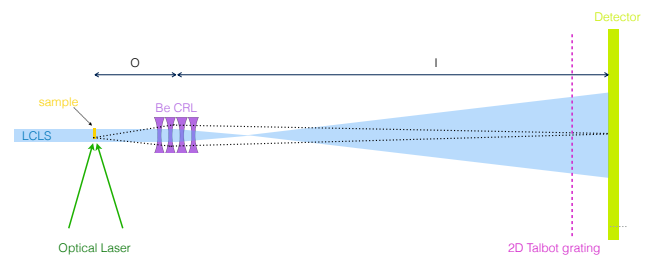


FIG. 9. Talbot Phase Imaging at MEC. The MXI is placed in a direct imaging geometry, where the Be lens stack images the sample onto an X-ray camera. A two dimensional checkerboard  $\pi$ -phase grating is placed at the distance of the first Talbot order before the camera.

white field correction (i.e., dividing the image of the sample by the white field of image when no sample is present) or by more sophisticated analysis method such as Principal Component Analysis [32, 38]. This is the analysis that is performed in the images in Figures 4, 6 and 7. However, a large enough number of white field images (the image of the X-rays on the detector when no sample is present) needs to be accumulated in order to improve the correction with a single shot. This is necessary because the Be CRL are chromatic and the FEL bandwidth jitters, which means that a small change of the incoming central photon energy changes the focal length of the stack, effectively changing the magnification onto the detector. A division of a single shot by a white field can thus be challenging. Talbot shearing interferometry allows to mitigate these lens artifacts and chromaticity.

Talbot interferometry has been widely used at FELs to determine the wavefront of the of the X-ray beam, and its focal properties in a single shot [37, 39, 40]. The method uses a two dimensional phase diffraction grating placed in the beam. At a specific distance behind the grating an “image” of the grating is reproduced. Analysis of the distortions, typically using Fourier methods [41] yields the differential phase in two orthogonal dimensions. These differential phases can be integrated to yield the full wavefront of the beam, and back-propagating to the focus yields the focal properties. It has been an important technique to quantify the focus in experiments where X-ray foci of order 100 nm were required.

We have combined this Talbot phase measurement technique with the direct imaging. The setup, which can be seen in Figure 9, is essentially the same as the direct imaging setup, with the addition of a Talbot grating. A checkerboard  $\pi$ -phase grating with a pitch of  $22.5\ \mu\text{m}$  was placed at the first Talbot distance in front of the imaging camera.

The raw image of the a shock propagating through Silicon with this setup is shown in Figure 10 (a). Both the elastic precursor, as well as the phase transformation to denser shocked state of Si, can be seen in the raw image. Overlaid on this image is the grid pattern introduced by the Talbot grating (an zoom region is shown in the inset) that is used to measure the phase. The two dimensional fringe pattern is analyzed by standard Fourier methods [41]. Since Talbot interferometry is a shearing interferometry method, the Fourier analysis results in the differential phase in the horizontal or vertical direction

depending on which Fourier peak is chosen.

There are many ways [37, 41–43] to integrate the differential phase and get the phase  $\phi(x, y)$  which each have their advantages and trade-offs. For the purpose of demonstration, in this paper, we use a fast and simple method [44]. Since at the first Talbot order the shear is small, we can approximate this as:

$$S_x(x, y) = \phi(x, y) - \phi(x - s, y) = s \frac{\partial \phi}{\partial x} \quad (1)$$

$$S_y(x, y) = \phi(x, y) - \phi(x, y - s) = s \frac{\partial \phi}{\partial y} \quad (2)$$

$$(3)$$

We then use the Fourier relation:

$$\mathcal{F}\left(\frac{\partial \phi}{\partial x}\right) = ik_x \mathcal{F}(\phi) \quad (4)$$

From this follows:

$$\phi = \mathcal{F}^{-1}\left(\frac{\mathcal{F}(S_x + iS_y)}{ik_x - k_y}\right) \quad (5)$$

which can be efficiently implemented using a fast Fourier transform and its inverse.

We used this method on a shock compressed silicon sample driven by the MEC long pulse laser, as detailed in Figure 10.

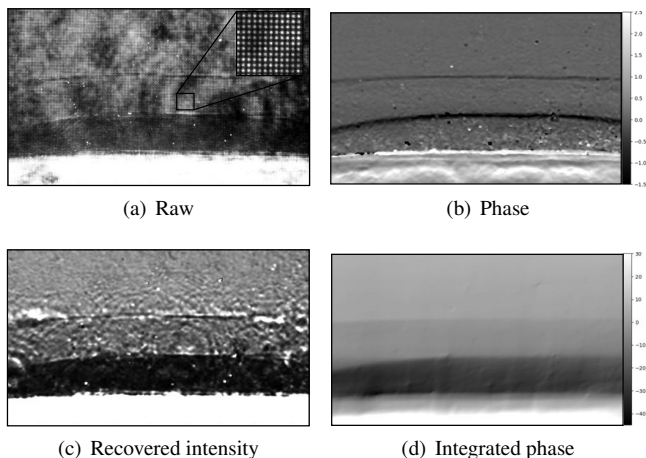


FIG. 10. (a) Raw Talbot phase image of a shock in a silicon sample. (b) Differential phase in  $y$ . (c) Recovered intensity change. (d) Integrated phase of the sample.

First an image was taken of the white field illumination (i.e., the beam without a sample in place) to use as a reference.

Then a measurement of the shock in the sample was taken. Figure 10 (a) shows the raw data of the shock, while 10 (b) shows the differential phase in the  $y$  direction. The reconstructed intensity is shown in Figure 10 (c). The structure of the Be lenses is highly visible in that image. In Figure 10 (d) we show the actual phase introduced by the sample; the structure in the intensity introduced by the lenses disappears, as it is not present in the phase. The phase change behind the elastic wave can clearly be seen, as well as the larger shift after the phase change.

The Fourier analysis of the initial two dimensional fringe pattern limits the resolution that can be attained due to the Nyquist–Shannon sampling theorem. In the data shown in Figure 10 the resolution of the phase measurement is approximately  $1.2 \mu\text{m}$ . However, the imaging geometry at MEC has the capability of magnification of up to  $\times 40$  at photon energies below 10 keV. Since we can easily resolve a  $4 \mu\text{m}$  Talbot pitch on the scintillator based detector, a resolution of  $8 \mu\text{m}$  in the phase measurement at the detector or  $\frac{8 \mu\text{m}}{40} = 200 \text{ nm}$  is achievable.

## VI. CONCLUDING REMARKS

In conclusion, we have developed an X-ray imaging diagnostic at MEC that is available to the user community. It can be used in combination with the MEC long pulse laser to, for example, image shock waves and phase transformation in materials over large field of view, and with the MEC short pulse laser system, to image its interaction with dense plasmas at high resolution. The diagnostic has a 200 nm spatial resolution, taking 50 fs (the pulse duration of the FEL) snapshot of excited HED samples, and can operate using photon energies ranging from 5 to 24 keV. In combination with the direct imaging geometry, a Talbot Imaging setup can be used to measure both intensity and phase changes introduced by a target with sub-micron resolution.

## ACKNOWLEDGMENTS

A.E.G. acknowledges support from the LANL Reines LDRD and from the DOE FES ECA, 2019. Use of the Linac Coherent Light Source (LCLS) SLAC National Accelerator Laboratory, was supported by the U.S. Department of Energy Office of Science, Basic Energy Science under Contract No. DE-AC02-76SF00515. The MEC instrument is supported also by the U.S. Department of Energy Office of Science, Fusion Energy Science under Contract No. DE-AC02-76SF00515, FWP 100106.

[1] M. Katayama, H. Shiraga, M. Nakai, T. Kobayashi, and Y. Kato, *Review of Scientific Instruments* **64**, 706 (1993).

[2] D. H. Kalantar, S. W. Haan, B. a. Hammel, C. J. Keane, O. L. Landen, and D. H. Munro, *Review of Scientific Instruments* **68**, 814 (1997).

- [3] F. J. Marshall, P. W. McKenty, J. a. Delettrez, R. Epstein, J. P. Knauer, V. a. Smalyuk, J. a. Frenje, C. K. Li, R. D. Petrasso, F. H. Séguin, and R. C. Mancini, *Physical Review Letters* **102**, 1 (2009).
- [4] D. G. Hicks, B. K. Spears, D. G. Braun, R. E. Olson, C. M. Sorce, P. M. Celliers, G. W. Collins, and O. L. Landen, *Review of Scientific Instruments* **81** (2010), 10.1063/1.3475727.
- [5] E. L. Dewald, O. L. Landen, L. Masse, D. Ho, Y. Ping, D. Thorn, N. Izumi, L. Berzak Hopkins, J. Kroll, A. Nikroo, and J. A. Koch, *Review of Scientific Instruments* **89**, 10G108 (2018), [https://pubs.aip.org/aip/rsi/article-pdf/doi/10.1063/1.5039346/16727284/10g108\\_1\\_online.pdf](https://pubs.aip.org/aip/rsi/article-pdf/doi/10.1063/1.5039346/16727284/10g108_1_online.pdf).
- [6] A. Do, C. R. Weber, E. L. Dewald, D. T. Casey, D. S. Clark, S. F. Khan, O. L. Landen, A. G. MacPhee, and V. A. Smalyuk, *Phys. Rev. Lett.* **129**, 215003 (2022).
- [7] T. a. Shelkovenko, D. B. Sinars, S. a. Pikuz, and D. a. Hammer, *Physics of Plasmas* **8**, 1305 (2001).
- [8] O. L. Landen, D. R. Farley, S. G. Glendinning, L. M. Logory, P. M. Bell, J. A. Koch, F. D. Lee, D. K. Bradley, D. H. Kalantar, C. a. Back, and R. E. Turner, *Review of Scientific Instruments* **72**, 627 (2001).
- [9] M. Oliver, C. H. Allen, L. Divol, Z. Karmiol, O. L. Landen, Y. Ping, R. Wallace, M. Schölmerich, W. Theobald, T. Döppner, and T. G. White, *Review of Scientific Instruments* **93**, 093502 (2022), [https://pubs.aip.org/aip/rsi/article-pdf/doi/10.1063/5.0091348/16601249/093502\\_1\\_online.pdf](https://pubs.aip.org/aip/rsi/article-pdf/doi/10.1063/5.0091348/16601249/093502_1_online.pdf).
- [10] A. Morace, L. Fedeli, D. Batani, S. Baton, F. N. Beg, S. Hulin, L. C. Jarrott, A. Margarit, M. Nakai, M. Nakatsutsumi, P. Nicolai, N. Piovella, M. S. Wei, X. Vaisseau, L. Volpe, and J. J. Santos, *Physics of Plasmas* **21**, 102712 (2014), [https://pubs.aip.org/aip/pop/article-pdf/doi/10.1063/1.4900867/14866977/102712\\_1\\_online.pdf](https://pubs.aip.org/aip/pop/article-pdf/doi/10.1063/1.4900867/14866977/102712_1_online.pdf).
- [11] D. S. Montgomery, A. Nobile, and P. J. Walsh, *Review of Scientific Instruments* **75**, 3986 (2004).
- [12] B. J. Koziowski, J. D. Sater, J. D. Moody, J. J. Sanchez, R. a. London, a. Barty, H. E. Martz, and D. S. Montgomery, *Journal of Applied Physics* **98** (2005), 10.1063/1.2133903.
- [13] J. a. Koch, O. L. Landen, B. J. Koziowski, N. Izumi, E. L. Dewald, J. D. Salmonson, and B. a. Hammel, *Journal of Applied Physics* **105** (2009), 10.1063/1.3133092.
- [14] Y. Ping, O. L. Landen, D. G. Hicks, J. a. Koch, R. Wallace, C. Sorce, B. a. Hammel, and G. W. Collins, *Journal of Instrumentation* **6**, P09004 (2011).
- [15] K. Nugent, T. Gureyev, D. Cookson, D. Paganin, and Z. Barnea, *Physical Review Letters* **77**, 2961 (1996).
- [16] P. Cloetens, W. Ludwig, J. Baruchel, J.-P. Guigay, P. Pernot-Rejmánková, M. Salomé-Pateyron, M. Schlenker, J.-Y. Buffière, E. Maire, and G. Peix, *Journal of Physics D: Applied Physics* **32**, A145 (1999).
- [17] P. Emma, R. Akre, J. Arthur, R. Bionta, C. Bostedt, J. Bozek, a. Brachmann, P. Bucksbaum, R. Coffee, F.-J. Decker, Y. Ding, D. Dowell, S. Edstrom, a. Fisher, J. Frisch, S. Gilevich, J. Hastings, G. Hays, P. Hering, Z. Huang, R. Iverson, H. Loos, M. Messerschmidt, a. Miahnahri, S. Moeller, H.-D. Nuhn, G. Pile, D. Ratner, J. Rzepiela, D. Schultz, T. Smith, P. Stefan, H. Tompkins, J. Turner, J. Welch, W. White, J. Wu, G. Yocky, and J. Galayda, *Nature Photonics* **4**, 641 (2010).
- [18] B. Nagler, B. Arnold, G. Bouchard, R. F. Boyce, R. M. Boyce, A. Callen, M. Campell, R. Curiel, E. Galtier, J. Garofoli, E. Granados, J. Hastings, G. Hays, P. Heimann, R. W. Lee, D. Milathianaki, L. Plummer, A. Schropp, A. Wallace, M. Welch, W. White, Z. Xing, J. Yin, J. Young, U. Zastra, and H. J. Lee, *Journal of Synchrotron Radiation* **22**, 520 (2015).
- [19] A. Snigirev, V. Kohn, I. Snigireva, and B. Lengeler, *Nature* **384**, 49 (1996).
- [20] B. Lengeler, C. Schroer, J. Tümmler, B. Benner, M. Richwin, a. Snigirev, I. Snigireva, and M. Drakopoulos, *Synchrotron Radiation News* **12**, 45 (1999).
- [21] B. Lengeler, C. Schroer, J. Tümmler, B. Benner, M. Richwin, A. Snigirev, I. Snigireva, and M. Drakopoulos, *Journal of Synchrotron Radiation* **6**, 1153 (1999).
- [22] B. Lengeler, C. G. Schroer, B. Benner, A. Gerhardus, T. F. Günzler, M. Kuhlmann, J. Meyer, and C. Zimprich, *Journal of synchrotron radiation* **9**, 119 (2002).
- [23] B. Nagler, A. Schropp, E. C. Galtier, B. Arnold, S. B. Brown, A. Fry, A. Gleason, E. Granados, A. Hashim, J. B. Hastings, D. Samberg, F. Seiboth, F. Tavella, Z. Xing, H. J. Lee, and C. G. Schroer, *Review of Scientific Instruments* **87**, 103701 (2016).
- [24] A. Schropp, R. Hoppe, V. Meier, J. Patommel, F. Seiboth, H. J. Lee, B. Nagler, E. C. Galtier, B. Arnold, U. Zastra, J. B. Hastings, D. Nilsson, F. Uhlen, U. Vogt, H. M. Hertz, and C. G. Schroer, *Scientific Reports* **3**, 1633 (2013).
- [25] F. Seiboth, A. Schropp, M. Scholz, F. Wittwer, C. Rödel, M. Wünsche, T. Ullsperger, S. Nolte, J. Rahomäki, K. Parfeniukas, *et al.*, *Nature Commun.* **8**, 14623 (2017).
- [26] L. M. Barker and R. E. Hollenbach, *Journal of Applied Physics* **43**, 4669 (1972), [https://pubs.aip.org/aip/jap/article-pdf/43/11/4669/7948385/4669\\_1\\_online.pdf](https://pubs.aip.org/aip/jap/article-pdf/43/11/4669/7948385/4669_1_online.pdf).
- [27] A. Schropp, P. Boye, J. M. Feldkamp, R. Hoppe, J. Patommel, D. Samberg, S. Stephan, K. Giewekemeyer, R. N. Wilke, T. Salditt, J. Gulden, a. P. Mancuso, I. a. Vartanyants, E. Weckert, S. Schöder, M. Burghammer, and C. G. Schroer, *Applied Physics Letters* **96**, 10 (2010).
- [28] Optique Peter, (2012), <https://www.optiquepeter.com/en/index.php>.
- [29] Advanced hCMOS Systems, (2021), <https://www.hcmos.com/>.
- [30] P. A. Hart, A. Carpenter, L. Claus, D. Damiani, M. Dayton, F.-J. Decker, A. Gleason, P. Heimann, E. Hurd, E. McBride, S. Nelson, M. Sanchez, S. Song, and D. Zhu, in *X-Ray Free-Electron Lasers: Advances in Source Development and Instrumentation V*, Vol. 11038, edited by T. Tschentscher, L. Patthey, K. Tiedtke, and M. Zangrando, International Society for Optics and Photonics (SPIE, 2019) p. 110380Q.
- [31] Q. Looker, A. P. Colombo, M. Kimmel, and J. L. Porter, *Review of Scientific Instruments* **91**, 043502 (2020), [https://pubs.aip.org/aip/rsi/article-pdf/doi/10.1063/5.0004711/14731052/043502\\_1\\_online.pdf](https://pubs.aip.org/aip/rsi/article-pdf/doi/10.1063/5.0004711/14731052/043502_1_online.pdf).
- [32] D. S. Hodge, A. F. T. Leong, S. Pandolfi, K. Kurzer-Ogul, D. S. Montgomery, H. Aluie, C. Bolme, T. Carver, E. Cunningham, C. B. Curry, M. Dayton, F.-J. Decker, E. Galtier, P. Hart, D. Khaghani, H. J. Lee, K. Li, Y. Liu, K. Ramos, J. Shang, S. Vetter, B. Nagler, R. L. Sandberg, and A. E. Gleason, *Opt. Express* **30**, 38405 (2022).
- [33] F.-J. Decker, K. L. Bane, W. Colocho, S. Gilevich, A. Marinelli, J. C. Sheppard, J. L. Turner, J. J. Turner, S. L. Vetter, A. Halavanau, C. Pellegrini, and A. A. Lutman, *Scientific Reports* **12**, 3253 (2022).
- [34] A. Halavanau, S. Carbajo, F.-J. Decker, A. Krasnykh, A. Lutman, A. Marinelli, C. Mayes, and D. Nguyen, in *Proc. IPAC'21*, International Particle Accelerator Conference No. 12 (JACoW Publishing, Geneva, Switzerland, 2021) pp. 365–368.
- [35] A. Schropp, R. Hoppe, V. Meier, J. Patommel, F. Seiboth, Y. Ping, D. G. Hicks, M. a. Beckwith, G. W. Collins, A. Higginbotham, J. S. Wark, H. J. Lee, B. Nagler, E. C. Galtier, B. Arnold, U. Zastra, J. B. Hastings, and C. G. Schroer, *Scientific Reports* **5**, 11089 (2015).

- [36] S. B. Brown, A. E. Gleason, E. Galtier, A. Higginbotham, B. Arnold, A. Fry, E. Granados, A. Hashim, C. G. Schroer, A. Schropp, F. Seiboth, F. Tavella, Z. Xing, W. Mao, H. J. Lee, and B. Nagler, *Science Advances* **5** (2019), [10.1126/sciadv.aau8044](https://doi.org/10.1126/sciadv.aau8044), <http://advances.sciencemag.org/content/5/3/eaau8044.full.pdf>.
- [37] M. Seaberg, R. Cojocaru, S. Berujon, E. Ziegler, A. Jaggi, J. Krempasky, F. Seiboth, A. Aquila, Y. Liu, A. Sakdinawat, H. J. Lee, U. Flechsig, L. Patthey, F. Koch, G. Seniutinas, C. David, D. Zhu, L. Mikeš, M. Makita, T. Koyama, A. P. Mancuso, H. N. Chapman, and P. Vagovič, *Journal of Synchrotron Radiation* **26**, 1115 (2019).
- [38] J. Hagemann, M. Vassholz, H. Hoeppe, M. Osterhoff, J. M. Rosselló, R. Mettin, F. Seiboth, A. Schropp, J. Möller, J. Hallmann, C. Kim, M. Scholz, U. Boesenberg, R. Schaffer, A. Zozulya, W. Lu, R. Shayduk, A. Madsen, C. G. Schroer, and T. Salditt, *Journal of Synchrotron Radiation* **28**, 52 (2021).
- [39] Y. Liu, M. Seaberg, D. Zhu, J. Krzywinski, F. Seiboth, C. Hardin, D. Cocco, A. Aquila, B. Nagler, H. J. Lee, S. Boutet, Y. Feng, Y. Ding, G. Marcus, and A. Sakdinawat, *Optica* **5**, 967 (2018).
- [40] S. Matsuyama, H. Yokoyama, R. Fukui, Y. Kohmura, K. Tamasaku, M. Yabashi, W. Yashiro, A. Momose, T. Ishikawa, and K. Yamauchi, *Opt. Express* **20**, 24977 (2012).
- [41] M. Takeda, H. Ina, and S. Kobayashi, *J. Opt. Soc. Am.* **72**, 156 (1982).
- [42] B. Nagler, A. Aquila, S. Boutet, E. C. Galtier, A. Hashim, M. S. Hunter, M. Liang, A. E. Sakdinawat, C. G. Schroer, A. Schropp, M. H. Seaberg, F. Seiboth, T. van Driel, Z. Xing, Y. Liu, and H. J. Lee, *Scientific Reports* **7**, 13698 (2017).
- [43] M. Makita, G. Seniutinas, M. H. Seaberg, H. J. Lee, E. C. Galtier, M. Liang, A. Aquila, S. Boutet, A. Hashim, M. S. Hunter, T. van Driel, U. Zastra, C. David, and B. Nagler, *Optica* **7**, 404 (2020).
- [44] K. S. Morgan, D. M. Paganin, and K. K. W. Siu, *Applied Physics Letters* **100**, 124102 (2012), [https://pubs.aip.org/aip/apl/article-pdf/doi/10.1063/1.3694918/14246351/124102\\_1\\_online.pdf](https://pubs.aip.org/aip/apl/article-pdf/doi/10.1063/1.3694918/14246351/124102_1_online.pdf).